Journal of Theoretical and Applied Vibration and Acoustics 10 (1) 67-85 (2024)

I S A V

Journal of Theoretical and Applied Vibration and Acoustics

journal homepage: http://tava.isav.ir

Vibro-acoustic behavior of unbalanced shaft-bearing-pedestal coupled system with bearing faults and looseness

Emadaldin Sh Khoram-Nejad [a], **Abdolreza Ohadi** [b,*]

[a] *Ph.D. Candidate, Acoustics Research Laboratory, Mechanical Engineering Department, Amirkabir University of Technology (Tehran Polytechnic), Tehran, IRAN*

[b] *Professor, Acoustics Research Laboratory, Mechanical Engineering Department, Amirkabir University of Technology (Tehran Polytechnic), Tehran, IRAN*

Research Article

ARTICLE INFO

Article history:
Received 26 April 2024

Received in revised form
15 June 2024

Accepted 5 July 2024

Available online 26 January 2025

Keywords:
Rolling element bearing

Bearing faults

Vibro-acoustic behavior

Pedestal looseness

Sound pressure level

ABSTRACT

Investigating the sound radiated from faulty rolling element bearings (REBs) in rotor-bearing systems is as crucial as studying their vibration characteristics. This approach offers experts and researchers a more comprehensive understanding of faulty REB behavior, enhancing fault diagnosis capabilities. This study examines the impact of bearing faults, pedestal looseness, and shaft eccentricity on the vibro-acoustic characteristics of REBs. Additionally, it assesses the influence of fault severity and compound fault scenarios on these behaviors. A 6-degree-of-freedom (DOF) dynamic model is developed for an SKF 6205 bearing, including the shaft, inner ring, outer ring, and pedestal. The Hertzian theory is employed to model contact between the bearing balls and inner/outer rings. The governing equations are solved using the Runge-Kutta method to determine the surface velocity of the REB components, yielding a 4.56% error compared to experimental results, demonstrating good agreement. Based on the surface velocity, the sound pressure level (SPL) is calculated by modeling the inner and outer rings as cylindrical sound sources. The results reveal that auditory and visual observation can identify shaft eccentricity, while sound is a more sensitive indicator of bearing faults. Detecting incipient faults remains challenging, regardless of whether vibration or sound measurement tools, such as accelerometers or sound level meters, are employed. Furthermore, phase portraits indicate that pedestal looseness and bearing faults, unlike shaft eccentricity, result in chaotic and unpredictable motion, which may explain the sudden failures often observed in industrial REBs.

1. Introduction

Fault diagnosis of rotating machinery is one of the most essential issues in various industries, and every component needs to be repaired and replaced after a while. Studying faults in rotating machines through modeling helps experts understand their behavior better. Bearings are one of the

* Corresponding author.
E-mail address: a_r_ohadi@aut.ac.ir (A.R. Ohadi)

http://dx.doi.org/10.22064/tava.2024.2027369.1238

most crucial components of rotating machinery systems. Sometimes, only after a certain period of operation of the bearings, they are replaced according to a specific schedule. But this will cause the healthy bearing that could have worked longer to be replaced unnecessarily. Therefore, it is very common for industrial experts to notice the fault in the bearings after hearing the working noise and send reports to replace it as soon as possible. REBs are a type of bearing whose working is based on the rolling principle. REBs comprise balls or rollers, an inner ring, an outer ring, and a cage. The REB structure, component precision, and lubrication status influence its performance and noises. Hence, exploring dynamic and bearing radiation noise modeling presents an intriguing area of investigation for comprehending fault behavior. REBs are always susceptible to failure because they transfer (bear) significant dynamic forces from the rotating parts of the system to the stationary parts. Another reason for the failure of REBs is their non-predictable motion and working conditions. Therefore, fault detection and diagnosis of REBs are of interest to both researchers and industrial technicians.

Investigating the effect of various faults on the change of nonlinear dynamic behavior of bearings/ rotor-bearing systems is crucial to understanding the nature of faults and providing a solution to diagnose the faults in rotating machines. It can be done using different methods, including experimental tests in the industry, in laboratories, or by modeling. Many studies have been performed on the vibration and dynamic behavior of REBs. In experimental tests or industrial conditions, studying all the desired conditions of faults in rotating machines is impossible. One of the important limitations of this is the life risks and financial costs that must be considered in experimental tests in industrial environments. Another limitation is a specific faulty state in a rotating machine during the experimental test, which may be impossible to detect. Therefore, dynamic modeling of different faults is popular in studying various faults. Most papers have investigated the nonlinear dynamic behavior of bearings/rotor bearing systems. Some papers model these systems as multi-degree of freedom (DOF) systems [1–4], and others model the bearings, especially REBs, as multi-body systems [5,6]. Additionally, certain studies have introduced techniques for generating faulty signals from the REBs [7,8] without modeling. In addition, a group of papers has introduced a new bearing system that reduces REB vibrations by floating it in oil [9,10]. Some other papers investigate the effect of rotor-baring faults on the vibration behavior of the system. For instance, An et al. [11] investigated a full-ceramic bearing-rotor system's dynamic model under thermally induced loosening between a full-ceramic bearing and its steel housings due to the thermal working condition. In another study by Jiang et al. [12], the effect of rub-impact and pedestal looseness on the nonlinear vibration behavior of a bearing-rotor system is investigated.

However, there are a few studies about sound radiated from a faulty REB. The noise resulting from the working of a faulty REB is usually due to the vibration of the surfaces of its components. For instance, consider an REB with a crack on its inner ring. An impact force is produced as each ball passes the crack location on the inner ring. Then, the balls, inner race, outer race, cage, and pedestal vibrate because of this impact force, which is harmonically applied to the rings when the shaft is rotating. Vibratory surfaces make air molecules oscillate, generating sound waves that create radiated noise, which can be heard. The literature on bearing research has scanty reports on REBs' acoustic performance. For example, [13,14] studied the acoustic properties of a hydrodynamic journal bearing using the oil film's SPL, which included the rotor imbalance and elastic deformation of the bearing liner. Yan et al. [15] proposed a method to compute noise in high-speed ceramic angular contact ball bearings. To the authors' best knowledge, the REB noise mechanism

and distribution characteristics have rarely been analyzed before. Studying the effect of various fault types on the radiated noise from rotor-bearing systems is necessary. Consequently, there remains a significant gap in the literature in the integrated study of both the vibration and acoustic behavior of faulty REBs in a complete shaft-bearing-pedestal system. This study addresses this gap by presenting a novel vibro-acoustic model that simultaneously examines both the acoustic and vibration behavior of the system. In this study, the effect of various severity of the REB's pedestal looseness, the inner and the outer ring faults, and the eccentricity of the shaft on the vibro-acoustic behavior of a rotor-bearing system is investigated for the first time.

In this paper, using a vibro-acoustic model, the vibration and acoustic behavior of a shaft-bearing-pedestal system are investigated. In section 2, the presented nonlinear dynamic model for 6-DOF and the modeling of bearing faults, unbalance, and pedestal looseness are described in detail. The present model encompasses a comprehensive analysis of REB, wherein the pedestal, inner ring, and outer ring are identified as the three essential components. After extracting the final equations, the displacement and velocity of the bearing surfaces are obtained by solving them. Next, to reveal how much noise the REB and its pedestal make, a cylindrical sound model can be considered using the obtained surface velocities of the inner, outer, and pedestal of the REB. Then, using the multi-sound-source principle, the total SPL of the REB was obtained. The accuracy of the modeling has been checked in section 3 by comparing the results with those in the literature. Then, the effects of various single and compound fault severity on the vibration and acoustic behavior of the presented model are investigated. Finally, section 4 concludes the results obtained in the last section in detail.

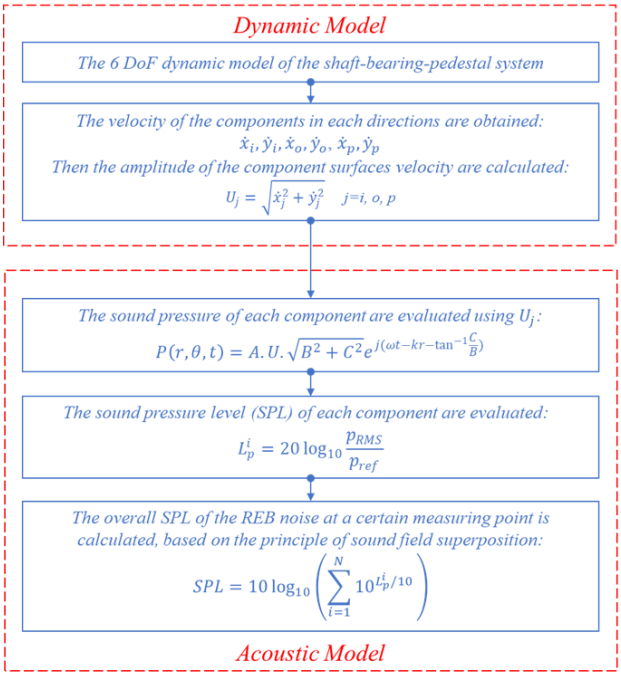

Fig. 1 The flowchart of the presented vibro-acoustic model of the shaft-bearing-pedestal system.

2. Methodology

In this research, dynamic and acoustic models are used, which will be explained in the next two subsections. After solving the REB dynamic equations using the Runge-Kutta method, the speed vectors of the REB's component surfaces are calculated and imposed on the acoustic model to calculate the SPL emitted by those components and the overall SPL emitted by the REB. Fig. 1 shows the presented vibro-acoustic model of the shaft-bearing-pedestal system.

2.1 Dynamic model

In this study, a shaft-bearing-pedestal dynamic model is considered as in [16]**,** with some changes and the addition of the pedestal looseness. The main changes in the dynamic model are briefly explained as follows:

- The model presented in [16] does not consider the eccentricity of the shaft. Their experiments only excite the REB with an external force in the y-axis.
- The model described in reference [16] does not account for the bearing pedestal looseness fault, which results in increased nonlinearity in the model's pedestal stiffness and damping.
- The damping and stiffness of the REB's pedestal in the x-axis are removed to simulate better the pillow block housing of the SKF 6205 REB.

The fault of the bearing's rings, called shaft current damage, is common in windmill turbines and subway motors, and scholars are interested in how it ig the shaft-bearing-pedestal (SBP) system. The dynamic models of the REB with fault characteristics are illustrated in Fig. 2. The model used in [16] without pedestal looseness is shown in Fig. 2-*a*. It models the pedestal and base connection by spring and damper in *x*- and *y*-directions using constant stiffness and damping coefficient values. Fig. 2-*c* indicates the model presented in this study, in which the foundation is considered a spring and damping coefficient only in *y*-direction. The equivalent coefficients can be expressed as follows [12]:

$$k_{py}^{Non} = \begin{cases} k_{py1} & y_p < 0 \\ k_{py2} & 0 \le y_p \le \delta \\ k_{py3} & \delta < y_p \end{cases} \tag{1}$$

$$c_{py}^{Non} = \begin{cases} c_{py1} & y_p < 0 \\ c_{py2} & 0 \le y_p \le \delta \\ c_{py3} & \delta < y_p \end{cases} \tag{2}$$

where δ is the looseness clearance and $y_p(t)$ is the pedestal displacement in the *y*-direction in the location of the REB. According to Fig. 3, the nonlinear piecewise functions of damping, c_{py}^{Non}, and stiffness, k_{py}^{Non}, express three states. During the operation, the bearing pedestal can be compressed to the base, $y_p < 0$, therefore the stiffness is more than usual and is defined by k_{py1}. When the bearing pedestal is not in contact with the base nor with the loose bolt, then $0 \le y_p \le \delta$ and the stiffness is zero, $k_{py2} = 0$. For $\delta < y_p$ the condition is the same as the normal connection without

the looseness and $k_{py3} < k_{py1}$. Additionally, c_{py1}, c_{py2}, and c_{py3} are damping coefficients of the pedestal-base connection in the three conditions mentioned above.

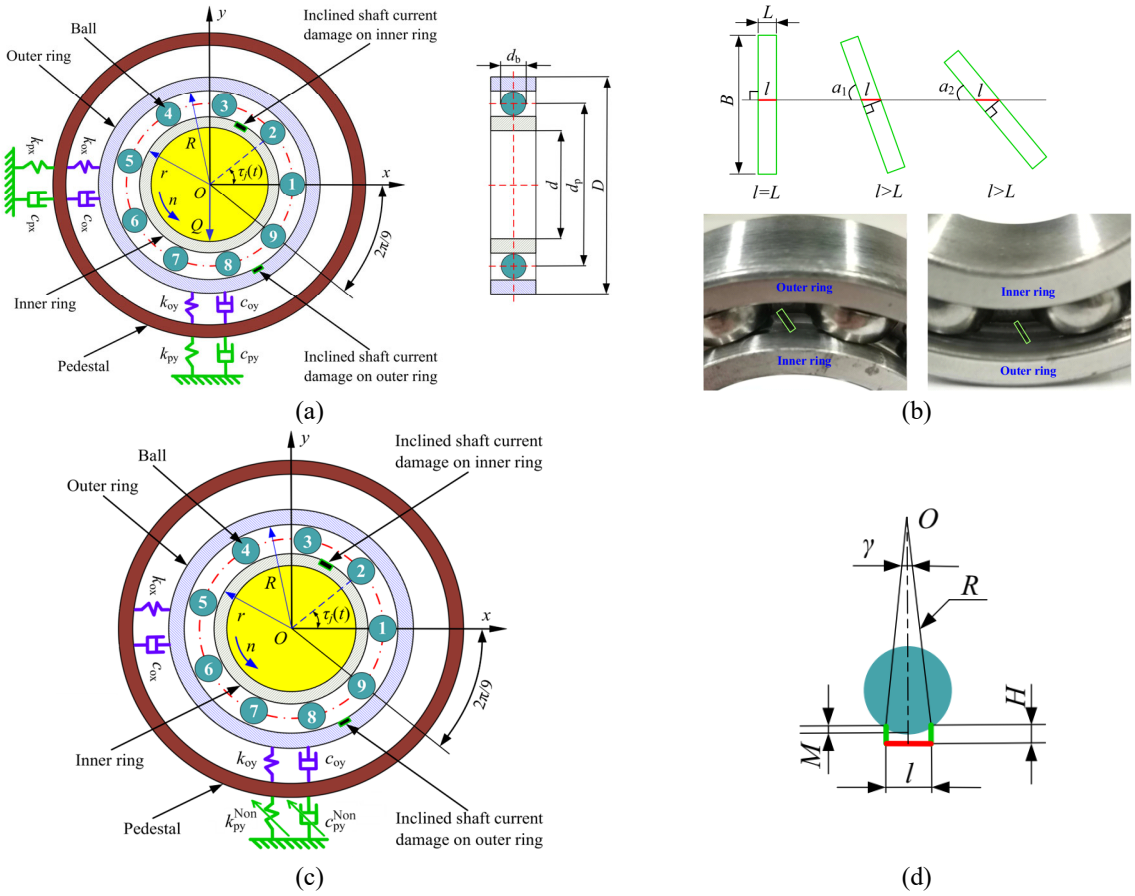

Fig. 2: REB and fault model characteristics; (*a*) the REB model in [16]; (*b*) bearing's ring fault geometrical parameters; (*c*) the presented REB model; (*d*) parameters related to the behavior of the balls passing the fault location.

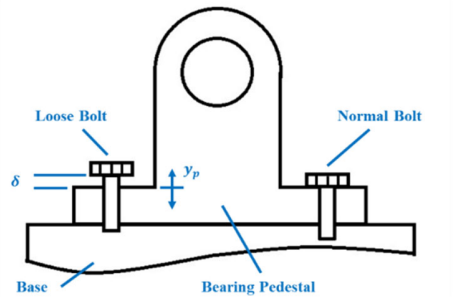

Fig. 3: Schematic diagram of bearing pedestal looseness model.

The REB differential equations of motion can be derived as:

$$\begin{cases} m_i\ddot{x}_i + F_{ix} + c_b(\dot{x}_i - \dot{x}_o) = m_i e\omega^2 \cos(\omega t) \\ m_i\ddot{y}_i + F_{iy} + c_b(\dot{y}_i - \dot{y}_o) = m_i e\omega^2 \sin(\omega t) \\ m_o\ddot{x}_o + c_{ox}(\dot{x}_o - \dot{x}_p) - c_b(\dot{x}_i - \dot{x}_o) + k_{ox}(x_o - x_p) - F_{ox} = 0 \\ m_o\ddot{y}_o + c_{oy}(\dot{y}_o - \dot{y}_p) - c_b(\dot{y}_i - \dot{y}_o) + k_{oy}(y_o - y_p) - F_{oy} = 0 \\ m_p\ddot{x}_p - c_{ox}(\dot{x}_o - \dot{x}_p) - k_{ox}(x_o - x_p) = 0 \\ m_p\ddot{y}_p + c_{py}\dot{y}_p - c_{oy}(\dot{y}_o - \dot{y}_p) + k_{py}y_p - k_{oy}(y_o - y_p) = 0 \end{cases} \quad (3)$$

where $x_p(t)$, $x_o(t)$, and $x_i(t)$ are the displacement of the pedestal, the outer, and the inner ring on the *x*-axis, and, $y_p(t)$, $y_o(t)$, and $y_i(t)$ are the displacement of the pedestal, and the outer and inner rings on the *y*-axis. Note that m_p, m_s, and m_o are the mass of the pedestal, the ring and shaft, and the outer ring, respectively. The damping coefficient and stiffness between the outer ring and the pedestal on the *x* and *y*-axis, and the damping coefficient of the ball are denoted by c_{ox}, k_{ox}, c_{oy}, k_{oy}, and c_b, respectively. Also, e is the eccentricity, and ω is the rotational speed of the shaft.

Using Hertzian contact theory [17], one can express the contact forces, including $F_{ix}(t)$, the contact force between the ball and the inner ring on the *x*-axis, $F_{iy}(t)$, the contact force between the ball and the inner ring on the *y*-axis, $F_{ox}(t)$, the contact force between the ball and the outer ring on the *x*-axis, and $F_{oy}(t)$ the contact force between the ball and the outer ring on the *y*-axis, as follows:

$$\begin{cases} F_{ix}(t) = \sum_{j=1}^{M} k_b \alpha_j^{\frac{3}{2}} H(\alpha_j) \cos(\tau_j) \\ F_{iy}(t) = \sum_{j=1}^{M} k_b \alpha_j^{\frac{3}{2}} H(\alpha_j) \sin(\tau_j) \\ F_{ox}(t) = \sum_{j=1}^{M} k_b \alpha_j^{\frac{3}{2}} H(\alpha_j) cos(\tau_j) \\ F_{oy}(t) = \sum_{j=1}^{M} k_b \alpha_j^{\frac{3}{2}} H(\alpha_j) sin(\tau_j) \end{cases} \quad (4)$$

where, M is the number of balls, k_b is the contact stiffness of the ball, $\alpha_j(t)$ is the total deformation, H is the Heaviside function, and $\tau_j(t)$ is the position angle of the j^{th} ball.

The position angle of the j^{th} ball is given by [18]:

$$\tau_j(t) = \omega_p t + \frac{2\pi(j-1)}{M}, \qquad j = 1,2,\dots,M \quad (5)$$

The total deformation can be calculated as given in Equation (6).

$$\alpha_j(t) = [x_i - x_o]\cos(\tau_j) + [y_i - y_o]\sin(\tau_j) - \frac{c_r}{2} - \beta_j \quad (6)$$

In Equation (6), c_r is the radial clearance and $\beta_j(t)$ is the additional displacement as given in Equation (7).

$$\beta_j(t) = \begin{cases} d_{max}\, sin\left(\frac{\pi}{\gamma}[mod(\phi, 2\pi) - \epsilon]\right) & \epsilon \le mod(\phi, 2\pi) \le \epsilon + \frac{\gamma}{2} \\ 0 & else \end{cases} \quad (7)$$

where d_{max}, is the maximum displacement of the ball when it falls into the damage and is defined as follows:

$$d_{max} = \frac{d_b}{2} - \sqrt{\frac{d_b^2}{4} - \frac{L^2}{4\cos^2(\frac{\pi}{2} - a)}} \quad (8)$$

In Equation (8), d_b, L, a, ϵ, γ, and ϕ are the ball diameter (Fig. 2-*a*), the length of the fault, the inclination angle, the initial angular offset of the fault of the j^{th} ball (Fig. 2-*b*), the damage angle corresponding to the displacement l, and the ring contact angle (Fig. 2-*d*), respectively.

If the contact deformation $\alpha_j(t)$ is positive, the contact force is calculated using the Hertzian contact theory; otherwise, no load is transmitted. It is defined by the Heaviside function as follows [16]:

$$H(\alpha_j) = \begin{cases} 0; & \alpha_j(t) \le 0 \\ 1; & \alpha_j(t) \ge 0 \end{cases} \quad (9)$$

where e, and ω are the eccentricity of the shaft and its rotational speed.

Solving Equation (3) with the Runge-Kutta method using ODE 45 in Matlab software results in state vectors, which include pedestal, inner, and outer ring velocities. Using these components' velocities, one may obtain the radiated noise from the REB in the next section.

To have an indicator for the displacements of the inner ring, outer ring, and bearing pedestal, one can define the total displacements D_j, velocities U_j, and accelerations A_j, as given in Equations (10-a) to (10-c), respectively.

$$D_j = \sqrt{x_j^2 + y_j^2}, \qquad j = i, o, p \quad (10\text{-}a)$$

$$U_j = \sqrt{\dot{x}_j^2 + \dot{y}_j^2}, \qquad j = i, o, p \quad (10\text{-}b)$$

$$A_j = \sqrt{\ddot{x}_j^2 + \ddot{y}_j^2}, \qquad j = i, o, p \quad (10\text{-}c)$$

2.2 Acoustic model

There are four components in the structure of the REBs: the inner ring, the outer ring, the rolling elements (balls or rollers), and the cage placed on a bearing pedestal. The system studied in this paper only considers the dynamics of the inner ring, the outer ring, and the pedestal of the bearing. Friction and impact noise radiated from the bearing components during the operation due to existing faults in the shaft-bearing-pedestal system. The REB's components are in constant motion, causing vibrations that create sound waves in the surrounding air. These sound waves travel through the environment and reach the human ear, allowing us to perceive the mechanical

movements of the REB. As components move and come into contact with each other, they create impacts and friction that contribute to the sounds we hear. Therefore, to analyze the noise characteristics of the REB system, the noise produced by each system component is investigated by measuring the amount of their surface vibration. The total radiation noise of the bearing is calculated by combining the noise from these three components. There are some assumptions on the medium around the bearing to calculate the radiation noise:

- The sound wave propagates through a perfect fluid with no energy loss.
- The medium is uniform and continuous without any sound disturbance.
- The medium and its vicinity remain adiabatic during sound wave propagation [15].

In the proposed dynamic model of REB, the DOFs are defined in the radial direction of the REB. REB components in the proposed model move cylindrically during vibration, leading to the use of a cylindrical sound source for measuring radiation noise.

The wave equation for the propagation of the small-amplitude wave in a perfect fluid is [19]:

$$\nabla^2 p - \frac{1}{c^2}\frac{\partial^2 p}{\partial t^2} = 0 \tag{11}$$

where, p, c, and t are sound pressure, sound velocity in the medium, and the time.

However, Equation (9) is expanded in cylindrical coordinates for the cylindrical wave sources. Therefore, one can rewrite Equation (11) as Equation (12). It is assumed that the x-axis coincides with the cylindrical axis. Thus, the sound pressure p is independent of the X coordinate.

$$\frac{\partial^2 p}{\partial r^2} + \frac{1}{r}\frac{\partial p}{\partial r} = \frac{1}{c^2}\frac{\partial^2 p}{\partial t^2} \tag{12}$$

In Equation (12), r is the distance between the observation point and the cylinder center. The far-field and out-of-cylinder solution for Equation (12) is given by [20]:

$$P(r,\theta,t) = A.U.\sqrt{B^2 + C^2}\, e^{j(\omega t - kr - \tan^{-1}\frac{C}{B})} \tag{13}$$

where;

$$A = \frac{\rho_0 c}{\frac{1}{4} + \left(\frac{2}{\pi k^2 a^2}\right)^2} cos\theta,$$

$$B = \frac{1}{\pi kr} + \frac{r}{\pi k a^2},$$

$$C = \frac{kr}{4} + \frac{4}{\pi^2 k^3 r a^2}$$

The surface velocity U_j in Equation (13) is obtained from the vibration analysis of the bearing in the previous section. See Equation (10-*b*).

The SPL of a certain sound source is measured by assuming a continuous time interval at a certain fixed position. It is also called the sound pressure RMS-value or the effective sound pressure and can be obtained as follows [13]:

$$p_{RMS} = \sqrt{\frac{1}{T}\int_0^T p^2 dt} \tag{14}$$

where p_{RMS} denotes the RMS value of the sound pressure; p, the instantaneous sound pressure, and T, the sampling time. The effective sound pressure level of i^{th} sound source at the measurement point can be calculated using Equation (15).

$$L_p^i = 20\log_{10}\frac{p_{RMS}}{p_{ref}} \tag{15}$$

where, $p_{ref} = 2 \times 10^5\, Pa$ is the SPL reference value. For N sound sources, Equation (16) calculates the overall SPL of the REB noise at a certain measuring point based on the principle of sound field superposition [15].

$$SPL = 10\log_{10}\left(\sum_{i=1}^{N} 10^{L_p^i/10}\right) \tag{16}$$

3. Results

The model used in this study is validated in the first sub-section. The vibro-acoustic behavior of REB is investigated in the next sub-sections. All the results, except in the first sub-section, are obtained from the presented model shown in Fig. 2-c. The pedestal-to-ground stiffness and damping coefficient are calculated as the piecewise nonlinear functions (Equations 1 and 2), in which, k_{py1}, k_{py2}, k_{py3}, c_{py1}, c_{py2}, and c_{py3} are considered $2040\, MN.m^{-1}$, $0\, MN.m^{-1}$, $20.4\, MN.m^{-1}$, $150\, N.s.m^{-1}$, $80\, N.s.m^{-1}$, and $200\, N.s.m^{-1}$, respectively.

3.1 Verification results

It is necessary to validate the model of the shaft-bearing-pedestal results. The model specification is stated in Table 1 for the model shown in Fig. 2-a and presented in [16].

For all the results given in this paper, the values in Table 1 are used unless it is mentioned in the description. The time responses of the system are shown in Fig. 4. The time response of the presented model in Fig. 4-*a* is like the simulation model and experimental system in Fig. 4-*b* and 4-*c* from reference [16]. The peak-to-peak values of the given model and those of the simulation and experimental system are $78.8\, m/s^2$, $78.8\, m/s^2$, and $82.63\, m/s^2$, respectively. The simulation results of [16] and the presented model have a modeling error of 4.63%, which is acceptable compared to the experimental results.

In the REB acoustic model, the SPL radiated from the REB is calculated using cylindrical sound sources for the inner ring, outer ring, and bearing pedestal. Besides other sound sources, this sound source model is validated in [15] by experimental measurements. Thus, the calculated velocities for the three components and the cylindrical sound source model used for determining the SPL are both valid.

Table 1: The specification of the shaft-bearing-pedestal system.

Parameter [Notation/ unit]	Value	Parameter [Notation/ unit]	Value
Shaft and inner ring mass $[m_i/\ kg]$	4.960	The length of the fault $[l/\ mm]$	0.975
Outer ring mass $[m_o/\ kg]$	0.048	The angle of the fault $[\alpha/\ °]$	60
Pedestal mass $[m_p/\ kg]$	8.560	Ball-ring contact stiffness $[k_b/\ MN.m^{-1.5}]$	93.9
Radial clearance $[c_r/\ \mu m]$	16	Ball-rings damping coefficient $[c_b/\ N.s.m^{-1}]$	300
Inner ring radius $[r/\ mm]$	15.547	Pedestal-to-ground stiffness in x-direction $[k_{px}/\ MN.m^{-1}]$	20.4
Outer ring radius $[R/\ mm]$	23.493	Pedestal-to-ground stiffness in y-direction $[k_{py}/\ MN.m^{-1}]]$	20.4
Ball diameter $[d_b/\ mm]$	7.938	Pedestal-to-ground damping in x- and y-direction $[c_{px}/\ N.s.m^{-1}]$	200
Number of the balls	9	Outer ring-Pedestal stiffness in x-direction $[k_{ox}/\ MN.m^{-1}]$	13.3
Rotational speed $[rpm]$	3000	Outer ring-Pedestal stiffness in y-direction $[k_{oy}/\ MN.m^{-1}]$	11.6
Eccentricity of the shaft $[e/\ mm]$	0.6	Outer ring-Pedestal damping in x- and y-direction $[c_{ox}/c_{oy}/\ N.s.m^{-1}]$	600

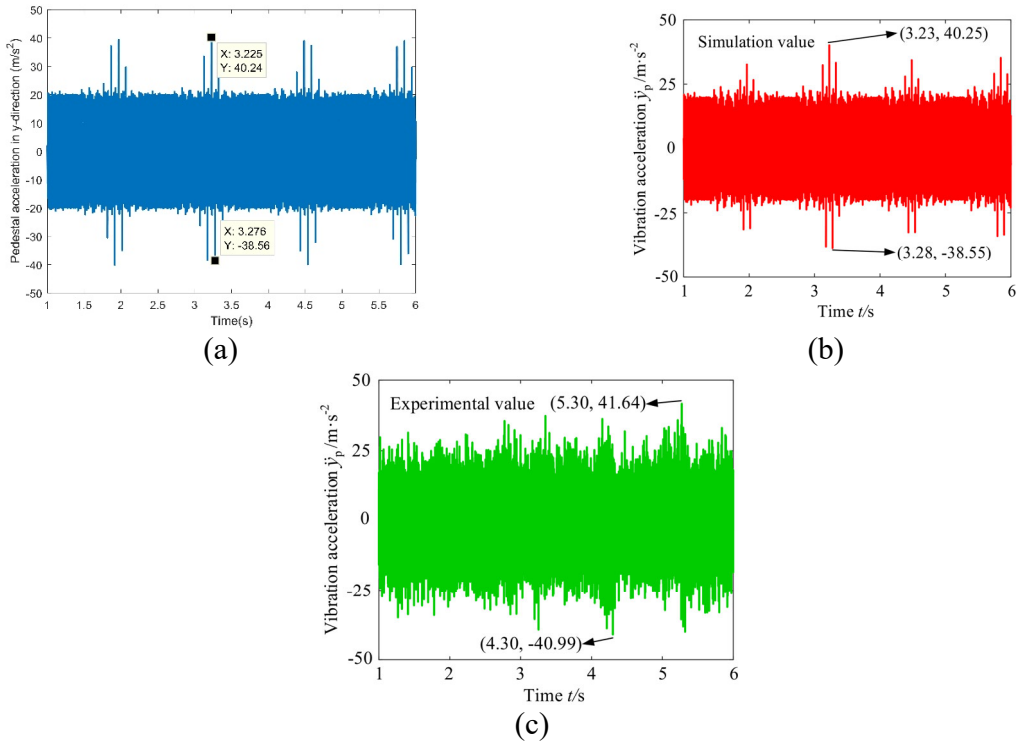

Fig. 4: The comparison between the time responses of (a) the presented model, (b) the simulation model of [16], and (c) the experimental sensors of [16].

3.2 Effect of eccentricity on the vibro-acoustic behavior of REB

Shaft eccentricity is common and exists in almost all real rotor systems with different working conditions. Therefore, investigating the effect of this factor on the vibro-acoustic behavior of rotors

is very important. A small amount of eccentricity in the rotors does not cause problems, and the experts, following the existing standards, always try to keep the eccentricity under its allowable level. The results are reported in Table 2 for a system with healthy REB. The SPL increased from $54.33\ dB$ to $70.93\ dB$ $(+\ 16.60\ dB)$ as the eccentricity of the shaft increased from $0.1\ mm$ to $1.0\ mm$. However, for this change in the shaft eccentricity, the pedestal displacement and acceleration are increased by $+0.4723\ mm$ and $+3.5905\ g$, respectively.

Table 2: Vibro-acoustic behavior of the healthy REB and different shaft eccentricities.

Shaft eccentricity	$\mathbf{1\ \mu m}$	$\mathbf{0.1\ mm}$	$\mathbf{0.3\ mm}$	$\mathbf{0.6\ mm}$	$\mathbf{1.0\ mm}$
$SPL\ (dB)$	16.31	54.33	61.48	66.82	70.93
$D_p\ (mm)$	0.0004	0.0530	0.1472	0.2856	0.4727
$A_P\ (g)$	0.0008	0.4144	1.0538	2.0076	3.5985

The nonlinear behavior of the REBs is also of interest to many researchers and is investigated in this study. A phase plot looks complicated, which is a sign of chaotic motion. It can be seen in Fig. **6** that in all cases, the movement of the bearing pedestal shows period-4 with the increase in the amount of shaft eccentricity, and no change in its behavior is observed. This fact is well-known in the literature [21]. In Fig. **6**-a, the amount of eccentricity is small, and the image indicates a simple periodic movement that results from low vibrations. With a significant increase in eccentricity, period-4 is observed. These four periodicities are observed in all eccentricity values.

Notably, increasing the eccentricity has the same effect as increasing the rotational speed (because the drag force increases at different rates in any case). Therefore, in this research, the impact of rotational speed on the vibro-acoustic behavior of the system has not been investigated.

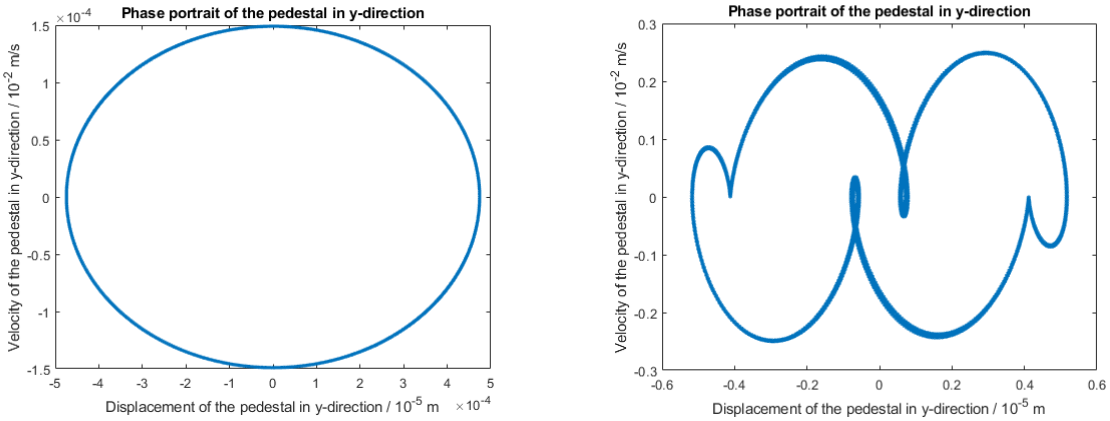

$(a)\ e = 1\ \mu m$ $(b)\ e = 0.1\ mm$

Fig. 5: Phase portraits of the pedestal in y-direction for different shaft eccentricities

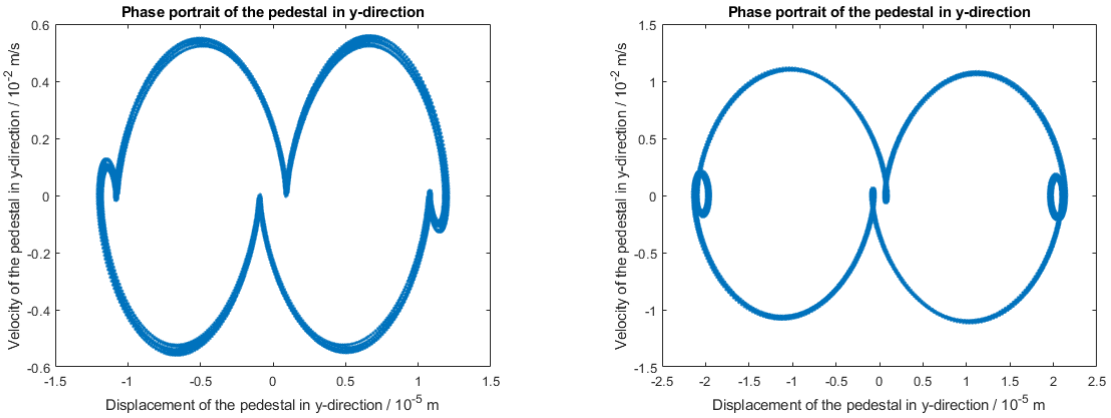

$(c)\ e = 0.3\ mm$ $(d)\ e = 0.6\ mm$

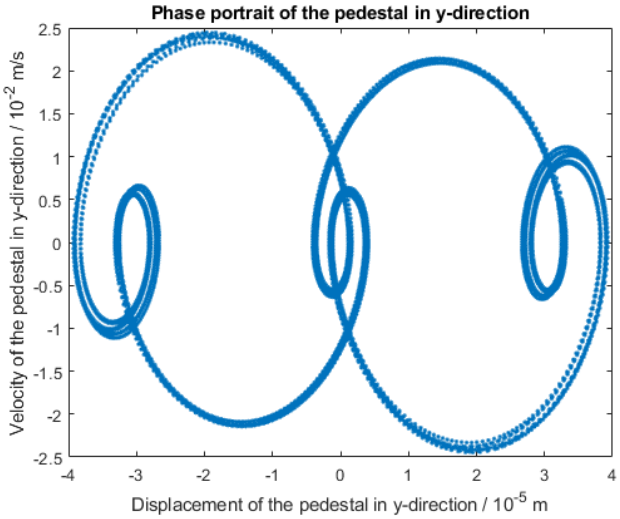

$(e)\ e = 1.0\ mm$

Fig. 6: Phase portraits of the pedestal in y-direction for different shaft eccentricities

3.3 Effect of bearing's fault severity on the vibro-acoustic behavior of the REB

In this sub-section, the effect of fault severity (in the means of fault length, L) on the vibro-acoustic behavior of the REB is investigated while the eccentricity is $0.1\ mm$. Table 3 and Table 4 show that the SPL of the healthy REB and the REB with severe fault on the inner ring and outer ring are different by $4.5\ dB$, and $1.52\ dB$, respectively. In the meantime, the differences between displacement of the pedestal for the healthy and faults on the inner and outer ring are $0.0011\ mm$ and $0.0003\ mm$, respectively. While, the pedestal acceleration becomes larger by about five and two times for inner and outer ring faulty REB, respectively.

Table 3: Effect of the different inner ring fault severities on the vibro-acoustic behavior of the REB.

Fault length	Without bearing fault	**1 *mm***	**5 *mm***	**10 *mm***
$SPL\ (dB)$	54.33	54.57	55.56	58.83
$D_p\ (mm)$	0.0530	0.0528	0.0535	0.0541
$A_P\ (g)$	0.4144	0.4365	1.0410	2.3446

Figures 6 and 7 indicate the phase portraits for different inner and outer ring fault severities. The inner and outer ring bearing faults are based on nonlinear contact theory. By increasing the share of the nonlinear force in the equations, which is achieved by increasing the faults, the phase portraits become more complicated, indicating chaotic motion.

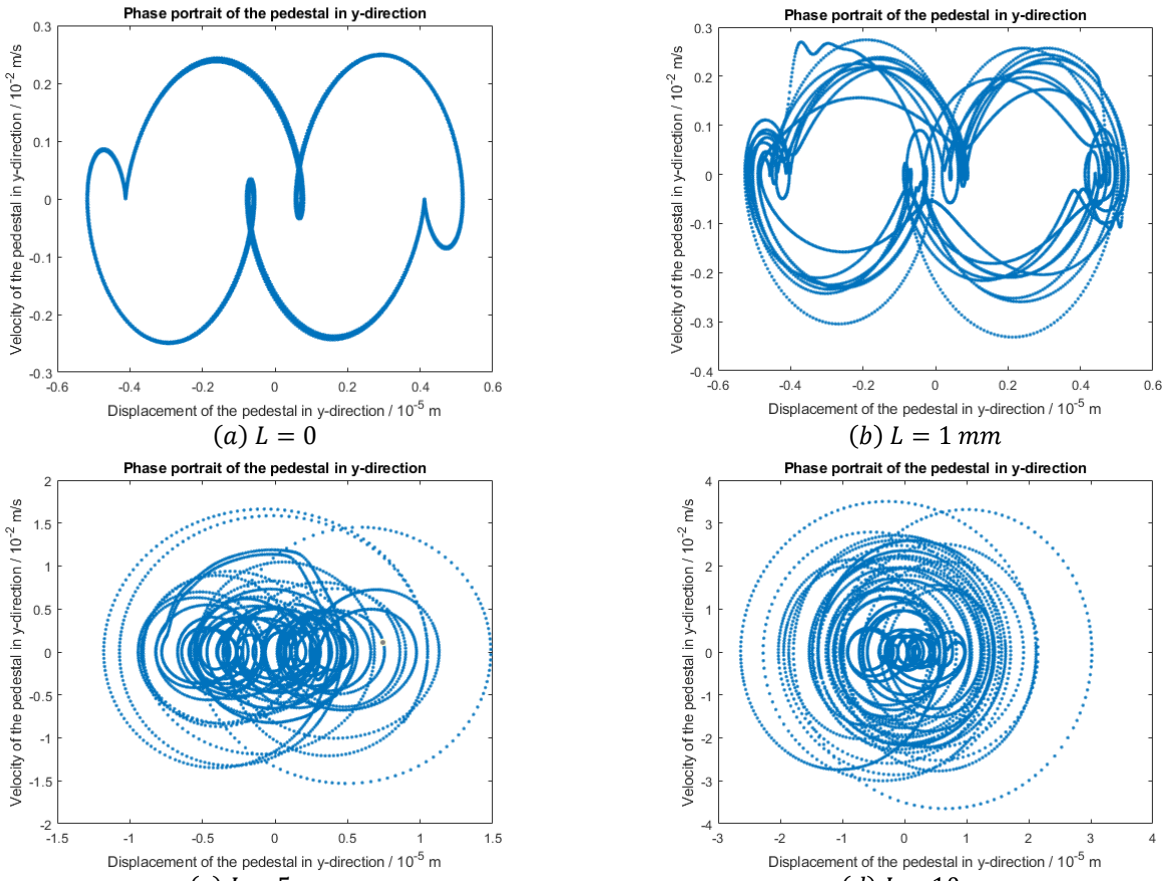

$(a)\ L = 0$ $(b)\ L = 1\ mm$

$(c)\ L = 5\ mm$ $(d)\ L = 10\ mm$

Fig. 7: Phase portraits of the pedestal in y-direction for different inner ring fault severity.

Table 4: Effect of the different outer ring fault severities on the vibro-acoustic behavior of the REB.

Fault length	Without bearing fault	**1 *mm***	**5 *mm***	**10 *mm***
$SPL\ (dB)$	54.33	54.54	54.95	55.85
$D_p\ (mm)$	0.0530	0.0528	0.0531	0.0533
$A_P\ (g)$	0.4144	0.4287	0.6364	0.8431

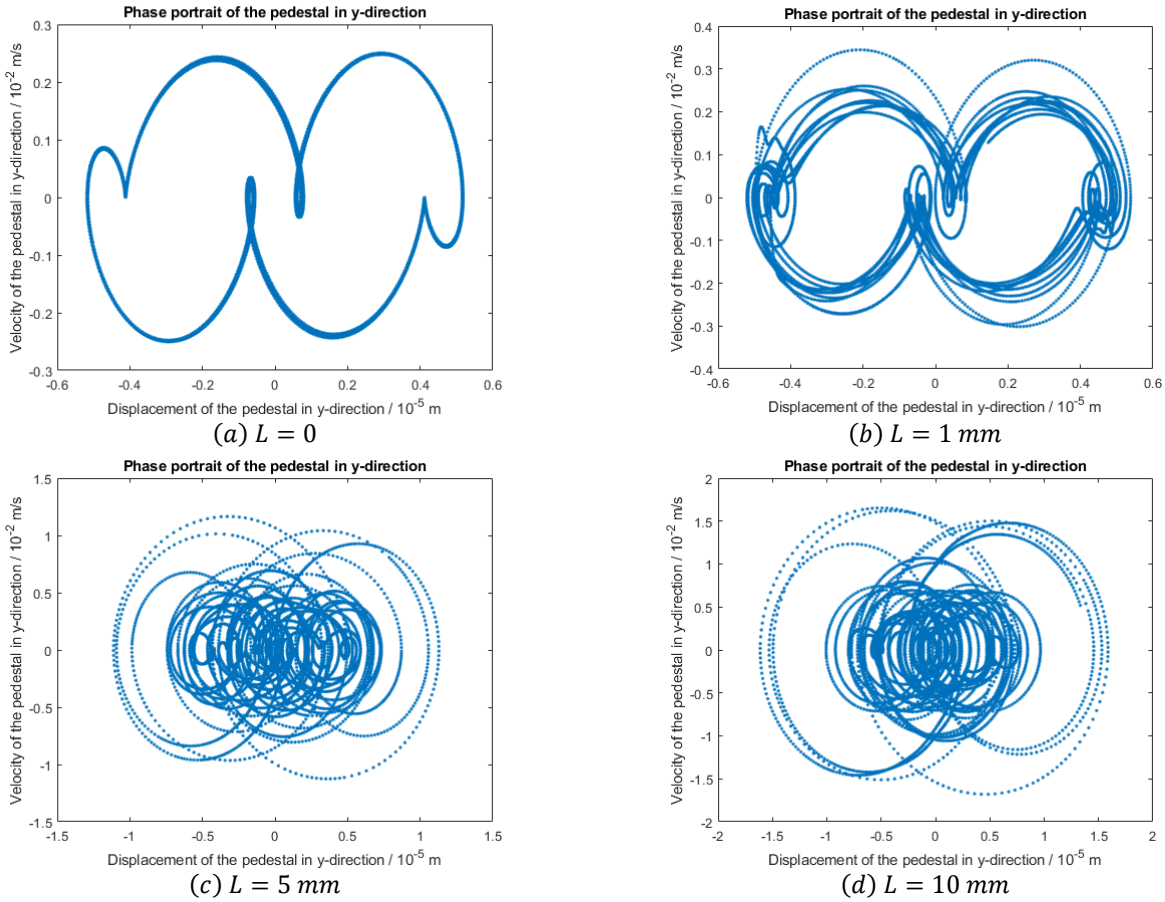

Fig. 8: Phase portraits of the pedestal in y-direction for different outer ring fault severity.

3.4 Effect of looseness on the vibro-acoustic behavior of the REB

Looseness in the REB pedestal is usually the cause of significant vibrations in rotating machines. In a healthy bearing and existence of 0.1 mm eccentricity, one can see the change in the acoustic and vibration variables of the bearing base in Table 5, with the increase in the amount of looseness clearance.

It can be observed from Table 5 that the SPL is changed by only $+0.52\ dB$, while the pedestal acceleration increased by $1.0495\ g$. The pedestal displacement, D_p, experiences a change of $0.0010\ mm$ and it is not visible to naked eyes.

Fig. 9 indicates the phase portraits for different looseness clearances. The motion of the rotor becomes chaotic when the looseness is increased. Also, it can be seen that the velocity of the pedestal in the y-direction has not changed significantly, but its displacement is very sensitive to the severity of looseness.

Table 5: Effect of the different looseness clearance on the vibro-acoustic behavior of the REB.

Looseness clearance	**5 μm**	**10 μm**	**15 μm**
$SPL\ (dB)$	54.30	54.55	54.82
$D_p\ (mm)$	0.0517	0.0521	0.0527
$A_P\ (g)$	1.7503	2.3900	2.7998

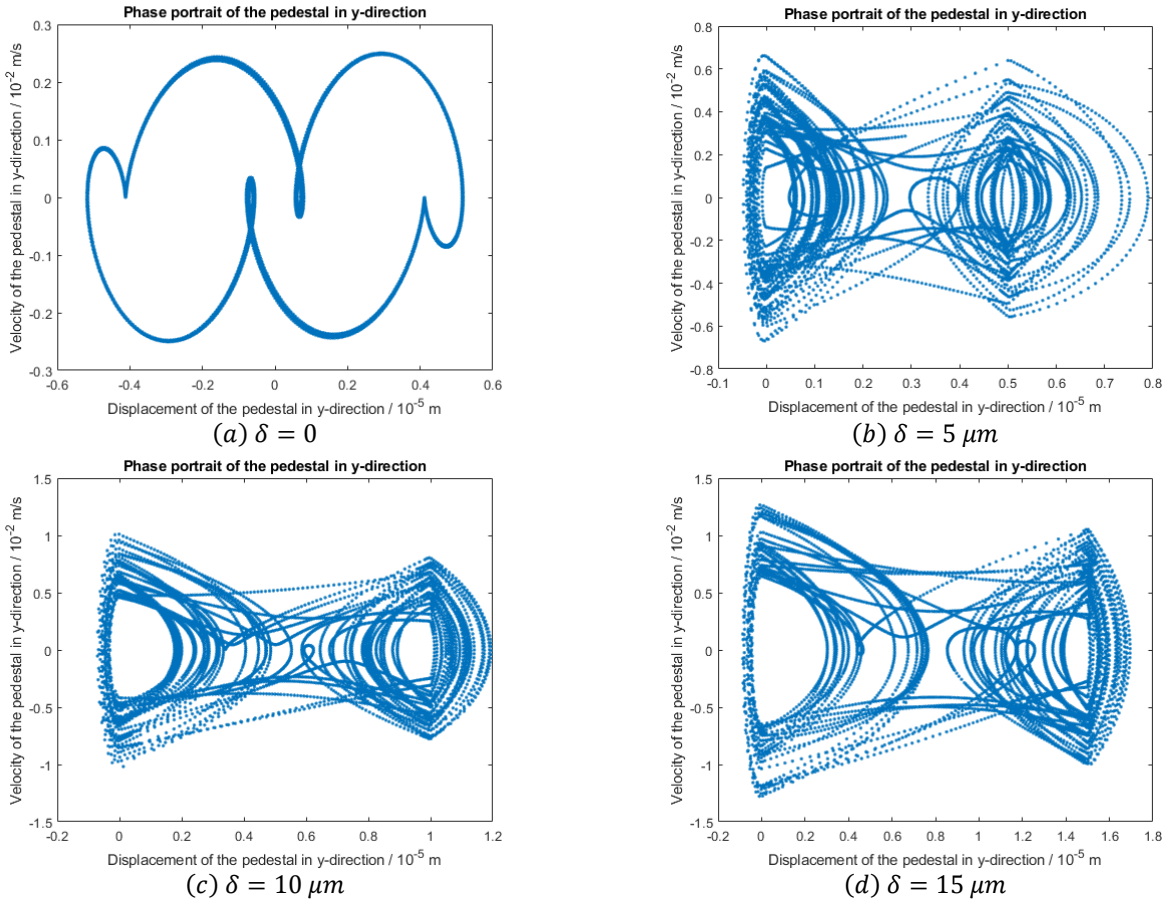

Fig. 9: Phase portraits of the pedestal in y-direction for different looseness severity.

3.5 Effect of looseness and bearing faults on the vibro-acoustic behavior of the REB

Investigating compound faults in rotating machines commonly occurring in the industry is crucial. In this section, the effect of fault length in the inner ring of the REB on its vibro-acoustic behavior has been investigated in the case of 0.1 mm eccentricity and 5 µm pedestal looseness.

According to Table 6, the SPL is changed by +1.39 dB, when the fault length in the inner ring increased to 6.8 mm. For a fault length of 6.9 mm, the SPL is significantly increased due to the

REB's failure. When comparing the vibro-acoustic behavior of the REB for inner ring fault lengths of 1 mm and 5 mm in Table 3 and Table 6, it is evident that loosening the bolts increases the pedestal accelerations. However, the pedestal displacement and SPL (below the 6.8 mm fault length) remain within a similar range.

Table 6: Effect of the different inner ring fault severities in the existence of the 5 μm pedestal looseness on the vibro-acoustic behavior of the REB.

Length of the fault	Without bearing fault	1 mm	5 mm	6.8 mm	6.9 mm
$SPL\ (dB)$	54.30	54.47	55.12	55.69	∞
$D_p\ (mm)$	0.0517	0.0518	0.0524	0.0523	∞
$A_P\ (g)$	1.7503	1.7021	2.4750	2.9018	∞

According to the phase portrait of the REB pedestal in Fig. 10, it is evident that the displacement and velocity of the bearing pedestal converge to infinity and indicate unstable dynamics when the eccentricity, looseness clearance, and the fault length in the REB inner ring are 0.1 mm, 1 µm, and 6.9 mm, respectively.

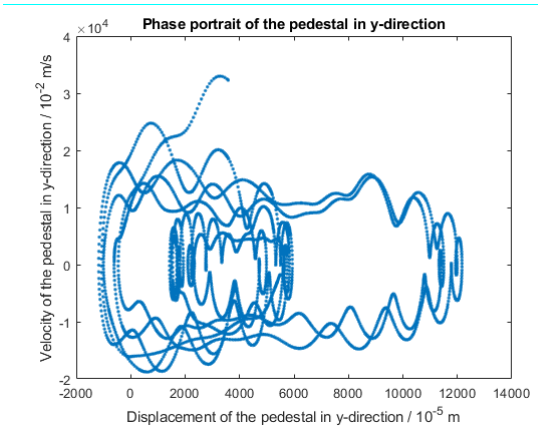

Fig. 10: Phase portraits of the pedestal in y-direction for looseness (with looseness clearance of $\mathbf{5}\ \boldsymbol{\mu m}$), inner ring bearing fault (with fault length of $\mathbf{6.9}\ \boldsymbol{mm}$), and $\mathbf{0.1}\ \boldsymbol{mm}$ eccentricity in the rotor system.

4. Conclusion

The effect of the bearing faults, pedestal looseness, and unbalanced shaft was investigated on the vibro-acoustic behavior of an SKF 6205 REB. The nonlinear contact between the bearing balls and the rings was considered using the Hertzian contact theory to model the bearing inner and outer ring faults. The pedestal looseness was modeled using a nonlinear spring and damper in the y-direction. The velocity and displacement of the REB model's three components, including the inner ring, outer ring, and bearing pedestal, were obtained by solving the nonlinear partial differential equations. The results of the dynamic modeling showed an error as small as 4.65% compared with the reference experimental results. The SPL in the far field was computed by assuming cylindrical sound sources for the three REB model components and their velocities. This

paper has investigated if fault diagnosis is possible visually or audibly using human senses or auxiliary tools like accelerometers and sound level meters. Some of the most important conclusions of this paper are:

1. The SPL changed by +16.60 dB when eccentricity increased by 0.9 mm (from 0.1 mm to 1.0 mm). The pedestal displacement and acceleration changed by +0.4723 mm and +3.5905 g, respectively. Therefore, it can be concluded that humans can easily detect shaft eccentricity without auxiliary tools.
2. It is fascinating to investigate whether humans can recognize bearing faults accurately with just their eyes or ears. When the inner ring fault length was increased by 10 mm, the SPL and pedestal displacement changed by 4.5 dB and 0.0011 mm. These changes are audible but not visible. For the REB with a faulty outer ring, the SPL and pedestal displacement increased by 1.52 dB and 0.0003 mm, which are neither audible nor visible to humans. Increasing fault length in the inner and outer rings of the REB caused pedestal acceleration to increase five and two times, respectively, which can be easily detectable by accelerometers. Therefore, the bearing faults are detectable using accelerometers and sound level meters.
3. The presence and increase of the bearing pedestal looseness from 5 μm to 15 μm led to an increase in the pedestal acceleration by 1.0495 g. Because the sound radiated from the impact between the loose bolt and the pedestal was not included in the acoustic modeling, it did not affect the calculated SPL, which was increased by 0.52 dB. It can be seen in the phase portraits that there are not many speed changes, unlike the extreme changes in the pedestal acceleration. Therefore, it is concluded that using the accelerometers is the best way to find the looseness in the bearing-rotor systems.
4. The presence of compound faults, including the inner ring fault of the REB, pedestal looseness, and shaft eccentricity, was also investigated. When the 0.1 mm shaft eccentricity and 5 μm pedestal looseness existed in the system, the increase in the inner ring fault length from 1 mm to 6.8 mm led to a sharp rise in the acceleration of the bearing pedestal (about +1.1997 g). The displacement of the bearing pedestal and the surrounding SPL did not change much. It is evident from the phase portrait that the system failed for a fault length of more than 6.9 mm and became completely unstable.
5. It was observed from the phase portraits that more severe faults led to more complicated phase portraits. Therefore, it can be concluded that the pedestal looseness and bearing faults lead to chaotic and non-predictable motion of REBs and the reason for sudden failures in REBs. In contrast, the eccentricity of the shaft does not change the system's behavior from periodic to chaotic.

References

[1] P. Yan, C. Yan, K. Wang, F. Wang, L. Wu, 5-DOF Dynamic Modeling of Rolling Bearing with Local Defect considering Comprehensive Stiffness under Isothermal Elastohydrodynamic Lubrication, Shock and Vibration, 2020 (2020) 9310278.

[2] X. Cheng, A. Wang, H. Yang, T. Zhang, C. Cao, G. Wu, Vibration analysis of a deep groove ball bearing with localized and distributed faults subject to waviness based on an improved model under time-varying speed condition, Journal of Vibration and Control, 29 (2023) 3259-3274.

[3] Y. Zhao, Y.-P. Zhu, J. Lin, Q. Han, Y. Liu, Analysis of nonlinear vibrations and health assessment of a bearing-rotor with rub-impact based on a data-driven approach, Journal of Sound and Vibration, 534 (2022) 117068.

[4] B. Changqing, X. Qingyu, Dynamic model of ball bearings with internal clearance and waviness, Journal of Sound and Vibration, 294 (2006) 23-48.

[5] M. Nakhaeinejad, M.D. Bryant, Dynamic Modeling of Rolling Element Bearings With Surface Contact Defects Using Bond Graphs, Journal of Tribology, 133 (2010).

[6] C. Mishra, A. Samantaray, G. Chakraborty, Bond graph modeling and experimental verification of a novel scheme for fault diagnosis of rolling element bearings in special operating conditions, Journal of Sound and Vibration, 377 (2016) 302-330.

[7] K.F. Al-Raheem, A. Roy, K. Ramachandran, D.K. Harrison, S. Grainger, Rolling element bearing faults diagnosis based on autocorrelation of optimized: wavelet de-noising technique, The International Journal of Advanced Manufacturing Technology, 40 (2009) 393-402.

[8] D. Ho, R. Randall, Optimisation of bearing diagnostic techniques using simulated and actual bearing fault signals, Mechanical systems and signal processing, 14 (2000) 763-788.

[9] S. Modaresahmadi, M. Ghazavi, M. Sheikhzad Saravani, Dynamic Analysis of a Rotor Supported on Ball Bearings with Waviness and Centralizing Springs and Squeeze Film Dampers, International Journal of Engineering, 28 (2015) 1351-1358.

[10] H.-l. Zhou, G.-h. Luo, G. Chen, F. Wang, Analysis of the nonlinear dynamic response of a rotor supported on ball bearings with floating-ring squeeze film dampers, Mechanism and Machine Theory, 59 (2013) 65-77.

[11] D. An, Y. Wei, A. Kumar, S. Ma, M. Shao, H. Zheng, Y. Wang, P. Xu, Dynamic analysis of full-ceramic bearing-rotor system under thermally induced loosening in aerospace applications, Engineering Failure Analysis, 159 (2024) 108080.

[12] M. Jiang, Y. Kuang, J. Wu, X. Li, Rub-Impact Detection in Rotor Systems with Pedestal Looseness Using a Nonlinearity Evaluation, Shock and Vibration, 2018 (2018) 7928164.

[13] B.-H. Rho, K.-W. Kim, Acoustical properties of hydrodynamic journal bearings, Tribology international, 36 (2003) 61-66.

[14] S. Bouaziz, T. Fakhfakh, M. Haddar, Acoustic analysis of hydrodynamic and elasto-hydrodynamic oil lubricated journal bearings, Journal of Hydrodynamics, Ser. B, 24 (2012) 250-256.

[15] H. Yan, Y. Wu, J. Sun, H. Wang, L. Zhang, Acoustic model of ceramic angular contact ball bearing based on multi-sound source method, Nonlinear Dynamics, 99 (2020) 1155-1177.

[16] F. Li, X. Li, J. Liu, D. Shang, H. Ma, Nonlinear vibration analysis of the shaft-bearing-pedestal coupled system with inclined shaft current damage, Nonlinear Dynamics, 111 (2023) 15853-15872.

[17] Q. Han, F. Chu, Nonlinear dynamic model for skidding behavior of angular contact ball bearings, Journal of Sound and Vibration, 354 (2015) 219-235.

[18] R. Tomovic, V. Miltenovic, M. Banic, A. Miltenovic, Vibration response of rigid rotor in unloaded rolling element bearing, International Journal of Mechanical Sciences, 52 (2010) 1176-1185.

[19] L.E. Kinsler, A.R. Frey, A.B. Coppens, J.V. Sanders, Fundamentals of acoustics, John wiley & sons, 2000.

[20] P. Aslani, S.D. Sommerfeldt, J.D. Blotter, Analysis of the external radiation from circular cylindrical shells, Journal of Sound and Vibration, 408 (2017) 154-167.

[21] N.A. Saeed, M.S. Mohamed, S.K. Elagan, Periodic, quasi-periodic, and chaotic motions to diagnose a crack on a horizontally supported nonlinear rotor system, Symmetry, 12 (2020) 2059.